AGU PUBLICATIONS

JGR

Journal of Geophysical Research: Oceans

RESEARCH ARTICLE

10.1002/2016JC011810

Key Points:
- Temperature and salinity fields of a soliton packet are recovered from seismic data
- An MCMC approach is developed to address the inversion and uncertainty estimation
- An accurate starting model is necessary for the strong sub-mesoscale variations

Supporting Information:
- Supporting Information S1

Correspondence to:
Q. Tang,
tqsh@scsio.ac.cn

Citation:
Tang, Q., R. Hobbs, C. Zheng, B. Biescas, and C. Caiado (2016), Markov Chain Monte Carlo inversion of temperature and salinity structure of an internal solitary wave packet from marine seismic data, *J. Geophys. Res. Oceans*, *121*, 3692–3709, doi:10.1002/2016JC011810.

Received 21 MAR 2016
Accepted 2 MAY 2016
Accepted article online 9 MAY 2016
Published online 2 JUN 2016

Markov Chain Monte Carlo inversion of temperature and salinity structure of an internal solitary wave packet from marine seismic data

Qunshu Tang[1,2], Richard Hobbs[2], Chan Zheng[3], Berta Biescas[4], and Camila Caiado[5]

[1]Key Laboratory of Marginal Sea Geology, South China Sea Institute of Oceanology, Chinese Academy of Sciences, Guangzhou, China, [2]Department of Earth Sciences, Durham University, Durham, UK, [3]College of Mathematics and Informatics, South China Agricultural University, Guangzhou, China, [4]Istituto di Scienze Marine, Consiglio Nazionale delle Ricerche, ISMAR Bologna, Italy, [5]Department of Mathematical Sciences, Durham University, Durham, UK

Abstract Marine seismic reflection technique is used to observe the strong ocean dynamic process of nonlinear internal solitary waves (ISWs or solitons) in the near-surface water. Analysis of ISWs is problematical because of their transient nature and limitations of classical physical oceanography methods. This work explores a Markov Chain Monte Carlo (MCMC) approach to recover the temperature and salinity of ISW field using the seismic reflectivity data and in situ hydrographic data. The MCMC approach is designed to directly sample the posterior probability distributions of temperature and salinity which are the solutions of the system under investigation. The principle improvement is the capability of incorporating uncertainties in observations and prior models which then provide quantified uncertainties in the output model parameters. We tested the MCMC approach on two acoustic reflectivity data sets one synthesized from a CTD cast and the other derived from multichannel seismic reflections. This method finds the solutions faithfully within the significantly narrowed confidence intervals from the provided priors. Combined with a low frequency initial model interpreted from seismic horizons of ISWs, the MCMC method is used to compute the finescale temperature, salinity, acoustic velocity, and density of ISW field. The statistically derived results are equivalent to the conventional linearized inversion method. However, the former provides us the quantified uncertainties of the temperature and salinity along the whole section whilst the latter does not. These results are the first time ISWs have been mapped with sufficient detail for further analysis of their dynamic properties.

1. Introduction

Seismic oceanography is widely used to study the ocean mesoscale to finescale structures due to its advantages of high lateral resolution (~10 m) and full depth imaging. With vessel steaming at 4–5 knots, the acquired seismic section is a deformed rolling snapshot of the actual ocean conditions [e.g., *Holbrook et al*., 2003; *Ruddick et al*., 2009; *Vsemirnova et al*., 2009]. *Tang et al*. [2015] showed how seismic oceanography can be used to estimate the phase-velocity of waves in the ocean, this movement can affect the imaging of the water structure [*Klaeschen et al*., 2009] however here, for simplicity, we have processed the data without accounting for the water movements. The seismic response is a proxy of vertical temperature and salinity gradients of the seawater [*Ruddick et al*., 2009; *Sallares et al*., 2009], however, they only tell us monographic features and relative strengths of thermohaline stratification, rather than absolute values of explicit physical characteristics which are required for oceanographic studies. Conventional linearized inversion of seismic data has been previously used to recover the principle physical properties of seawater [*Wood et al*., 2008; *Papenberg et al*., 2010; *Biescas et al*., 2014].

Temperature, salinity and pressure/depth $(T,\ S,\ p)$ are the three fundamental parameters of seawater that control the acoustic velocity and density, and therefore the acoustic reflection. From a hydrographic perspective the water density, $\rho(T,S,p)$, is one of the dominating factors driving ocean motions over a wide range of scales. For an internal solitary wave (ISW), the density stratification, which is described by buoyancy frequency N, is a crucial factor regulating the ISWs from generation, through propagation and deformation, and eventually to their dissipation. From a seismological aspect, reflections from the seawater are the convolution of a seismic impulse response (or source wavelet) with the acoustic impedance, Z, contrast profile

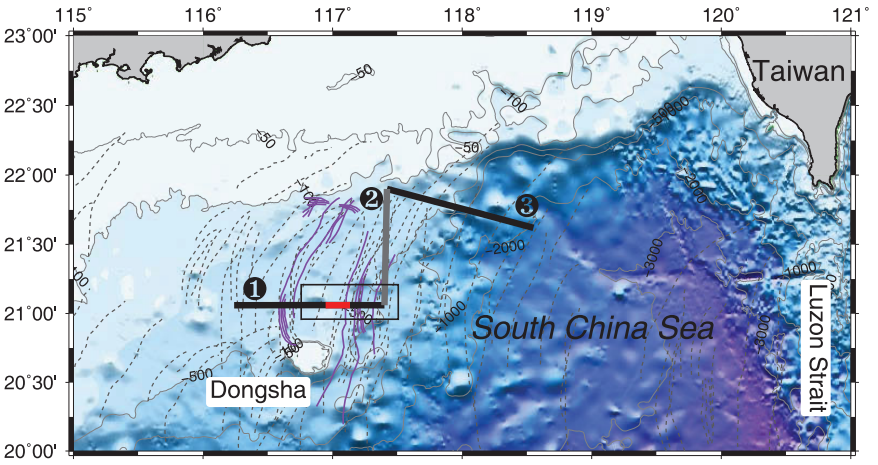

Figure 1. Bathymetry of the NE South China Sea. Thick lines are the seismic lines of the cruise in July 2014. Line 1 and 3 (black) are round-trip and line 2 (gray) is single trip. The box shows the study region in Figure 4. Red line shows the seismic subsection in which an ISW packet was observed on 13 July 2014. Gray dashed curves are surface spread of the satellite imaged ISWs modified from *Zhao et al.* [2004]. Purple curves are the ISW crests from satellite image on the same day of seismic survey.

(or reflection coefficient series), which is the vertical difference between any two adjacent water layers. Here the impedance Z is the product of acoustic velocity c and water density ρ, i.e., $Z(T,S,p)=c\cdot\rho$. Considering both the acoustic velocity c and water density ρ are the nonlinear functions of $(T,\ S,\ p)$ determined by the equation of state of seawater [*Millero*, 2010], the seismic image is ultimately determined by $(T,\ S,\ p)$ as a nonlinear forward problem [*Ruddick et al.*, 2009]. Therefore, in theory, it should be possible to recover temperature and salinity from the seismic data as a geophysical inversion problem, while the depth can be determined from seismic wave travel time. Once $(T,\ S,\ p)$ are known other parameters can be computed e.g., potential density (σ_0 in this study).

So far, two approaches have been applied to recover T and S from seismic data: full waveform inversion [*Wood et al.*, 2008; *Kormann et al.*, 2011; *Bornstein et al.*, 2013; *Padhi et al.*, 2015] or the computation of intermediate variables (c or Z) derived from seismic reflection coefficients to invert T and S simultaneously [*Papenberg et al.*, 2010; *Biescas et al.*, 2014]. Both approaches work well with T and S accuracies varying from 0.03 to 0.1°C and 0.01 to 0.1 psu, respectively. However, the error (defined as the differences between CTD/XBT values and seismic inverted results at same depths) used to test the accuracy of these results assumes the observed CTD/XBT data are correct which may not be true. For instance, the hydrographic observation and seismic result will never match if there is a depth shift between these two independent data sets, even though the inversion method is perfect. This depth shift can be caused by variations in the descent rate of the XBT (5 m uncertainties) [*Zhang et al.*, 2012] or the time delay between acquiring seismic data and a coincident CTD cast. So we cannot distinguish which one is better because we never really know the true value. To help reconcile these differences we introduce a robust method to estimate the uncertainties in the inversion process, hence characterize the range of values within which the true value is expected to lie. We use a Bayesian Markov Chain Monte Carlo (MCMC) method to qualify the uncertainties (σ), which is widely used in many scientific areas.

In this study we will recover the finescale *T-S* structure based on the Bayesian statistical inference for a well-developed ISW packet captured near Dongsha Plateau (Figure 1). The statistical problem, or the so-called "inversion," is to find the distribution of possible solutions near the smoothed starting *T-S* model that models the observed acoustic reflectivity. To achieve this goal, we first develop an MCMC approach to describe the relationship between *T-S* and acoustic reflectivity and test the method on the synthetic seismic data computed from a CTD cast. Then we apply this method to the real seismic data over an ISW packet to recover the *T-S* field. We compare our new method against a recently published method [*Biescas et al.*, 2014]. The primary objective of this study is to extract quantified parameters so we can test the limits of seismic oceanography for constraining processes in the ocean such as diapycnal mixing.

Similar to the previous methods [*Papenberg et al.*, 2010; *Biescas et al.*, 2014], the MCMC approach developed in this study relies on the smoothed initial model from in situ hydrographic observations, e.g., XBT or CTD

casts, due to the band-limited nature of seismic data. Using a smooth *T-S* initial model from sparse XBT casts (supporting information Figure S1), the MCMC retrieved *T-S* fields do not match hydrographically observed ISWs, where the *T-S* fields are strongly distorted and the isothermals/isopycnals are in typically "sech^{2}" shape [*Ramp et al*., 2004]. Therefore, the initial models from sparse XBT casts only (mesoscale) are not dense enough to capture the detailed background of ISW field (sub-mesoscale). In this study, we focus on the *T-S* field recovery using an improved initial model composed from both XBT casts and shape of the seismic reflections.

2. Water Properties and Study Region of ISWs

Temperature, salinity, and pressure are the fundamental parameters that describe the water column. In the sub-mesoscale to finescale ISW fields, the strong dynamic process often causes severe deformation of the ocean thermal, haline, and pycnal stratification. A series of macroscopic events, such as generation, propagation, disintegration, polarity conversion, and dissipation, during ISW evolution may accompany many small scale processes as mixing, gravitational instability and wave breaking [*Lien et al*., 2014]. Seismic data have the potential of providing detailed properties of the finescale structures, with resolutions of 10–100 m in both lateral and vertical dimensions, which will reveal new insights about intrinsic dynamic and mixing [e.g., *Biescas et al*., 2014].

ISWs in the northern South China Sea are generated at Luzon Strait by the interaction between tidal forcing and Luzon ridge [*Buijsman et al*., 2010]. After propagating across the deep basin to the coastal region of the South China Sea, they are well-developed and easily observed in the shallower water area, especially on Dongsha Plateau, by physical oceanographic mooring arrays, echo-sounder, shipboard radar, and satellite [e.g., *Orr and Mignerey*, 2003; *Zhao et al*., 2004; *Ramp and Tang*, 2011; *Cai et al*., 2012]. Based on these observed data, ISWs were extensively studied in terms of generation mechanisms, propagation behavior, spatial-temporal distribution, force exerted, etc. [*Ramp et al*., 2004; *Cai et al*., 2006; *Zheng et al*., 2007; *Huang et al*., 2014]. *Tang et al*. [2014b] used the marine multichannel seismic reflection technique to observe the ISWs in the NE South China Sea and derive their spatial structures and some kinematic parameters.

Following the initial success, a second multichannel seismic reflection survey was carried out in July 2014 near Dongsha Plateau (Figure 1) [*Tang et al*., 2015]. We used a source array composed of two Sercel GI guns fired at 2000 psi and in harmonic mode with matched generator/injector chamber sizes of 105 cu. in. The near offset (source-receiver distance) was adjusted to 90 m to reduce the blank zone at the top of the section to ~40 m. In order to increase the fold of cover and thus the signal-to-noise ratio (SNR), a shot interval of 25 m was used. The seismic source was towed at 5 m depth so that useful frequencies up to the ghost notch at 150 Hz would be generated. A Sercel Seal oil filled hydrophone streamer with 120 channels (1500 m length, 12.5 m spacing) was also towed at 5 m depth.

3. Methodology

There are three steps required to achieve the objective of producing estimates of temperature and salinity with quantified uncertainty: true-amplitude seismic data processing; salinity estimation from XBT data; and modeling using the MCMC approach. The second step is not mandatory if there are salinity data, e.g., from (X)CTD casts, for the starting model.

3.1. True-Amplitude Seismic Data Processing

The seismic image does not represent a specific physical variable but the amplitude and phase of the mapped events gives the relative reflection strength. However, the physically meaningful parameters of reflectivity *R*, which will be used to recover the *T-S* field, can be obtained if care is taken to compensate for signal distortion and scaling during processing. Standard true-amplitude data processing procedures to produce the final reflectivity include: (1) defining geometry, (2) amplitude correction, (3) noise attenuation, (4) common midpoint sorting and velocity analysis, (5) normal moveout (NMO), dip moveout (DMO), stacking and migration, and (6) deconvolution and amplitude calibration. Specific details of these steps are presented below.

1. Defining geometry setting: the geometry was referenced to a UTM Cartesian grid using the shot location data and field acquisition parameters to create the coordinates for the multichannel seismic data.
2. Amplitude correction include three primary factors that affect the acoustic amplitude: (1) angles of wave incidence because of the varying source-receiver offsets; (2) receiver directivity depending on the physical configurations of the hydrophone array for each channel of the streamer; and (3) spherical divergence of the transmitted acoustic wave [*Sheriff and Geldart*, 1995; *Biescas et al*., 2014]. We applied the necessary corrections to the common shot gathers to preserve the amplitude (supporting information Figure S2).
3. The main purpose of noise attenuation is to enhance the SNR. Three steps were carried out including: (1) bad trace removal, traces with poor SNR were removed; (2) band-pass filtering using a zero-phase 15–120 Hz filter; and (3) the direct wave is suppressed using an eigenvector filter [*Jones and Levy*, 1987].
4. Seismic data were sorted from shot gathers into CMP gathers. Because the stacking fold (30) was low especially near the surface, the super-gathers from four neighboring CMP gathers were combined for velocity analysis.
5. Normal Moveout (NMO) was applied to compensate for offset dependent moveout so as to make the reflections within each CMP gathers were flat. Dip Moveout (DMO) was applied after NMO to reduce lateral blurring of the final image at steep dips prior to stacking and poststack migration. Such a procedure is equivalent to the prestack migration where the acoustic velocity is nearly constant as it true for water. An FX deconvolution, which is dip sensitive, is used to attenuate random noise to increase the SNR.
6. Deconvolution and amplitude calibration: First, a sparse spike deconvolution was used to remove the source term [*Sacchi*, 1997], which was based on a minimum phase source wavelet extracted from the seismic data set. Second, a scaling factor was applied to retrieve the true reflectivity R:

$$R=\frac{Z_2-Z_1}{Z_2+Z_1}=\frac{c_2\rho_2-c_1\rho_1}{c_2\rho_2+c_1\rho_1} \tag{1}$$

where Z_1, c_1, ρ_1 and Z_2, c_2, ρ_2 are the impedance, acoustic velocity, density of the first and second medium, respectively. The seafloor reflection and its first multiple were measured to calibrate the amplitude (supporting information Figure S3) [*Warner*, 1990]:

$$R=K\cdot A;\;\; K=\frac{A_m}{A_{sf}^2}=\frac{R_{sf}}{A_{sf}} \tag{2}$$

where K is the correction coefficient, A is the amplitude of seismic image, A_{sf} and A_m are the amplitudes of seafloor reflection and its multiple, respectively, and R_{sf} is the reflection coefficient of seafloor.

Figure 2 shows the computed seawater reflectivity, which will be used for *T-S* recovery via equation (1), from the migrated seismic image.

3.2. Salinity and Temperature Models

Since we only have temperature data from the in situ XBT profiles, we have to infer the salinity before density and acoustic velocity calculation using the equation of state of seawater. Here a nonlinear neural network algorithm [*Ballabrera-Poy et al*., 2009] was applied to derive the *T-S* relation as presented by *Kormann et al*. [2011] and *Biescas et al*. [2014].

Historical CTD casts from the World Ocean Database (2013) are used to construct the *T-S* relation for this region. The data are selected using two criteria, spatially (116°E–119°E, 20°N–22°N) and temporally between May to September, covering the spatio-temporal parameters of this cruise. This ensures the CTD data are, as much as possible, relevant to this experiment in both regional and seasonal terms. The selected data are randomly divided into two groups (training data and validation data). A neural network with a single hidden layer and 50 neurons is trained using the *T-S* anomalies after subtracting the means to derive the salinity (Figure 3). Furthermore, a neural network table (supporting information Figure S4) is prepared for the conventional linearized inversion [*Biescas et al*., 2014] using acoustic impedance as the intermediate parameter, called the IMP method hereafter.

As aforementioned, the smooth *T-S* model from the sparse XBTs can not be used to recover the horizontal sub-mesoscale to finescale *T-S* fields of ISWs. However, the seismic image itself has good lateral resolution which could provide excellent constraints on the *T-S* extrapolation from the XBT sites if the seismic

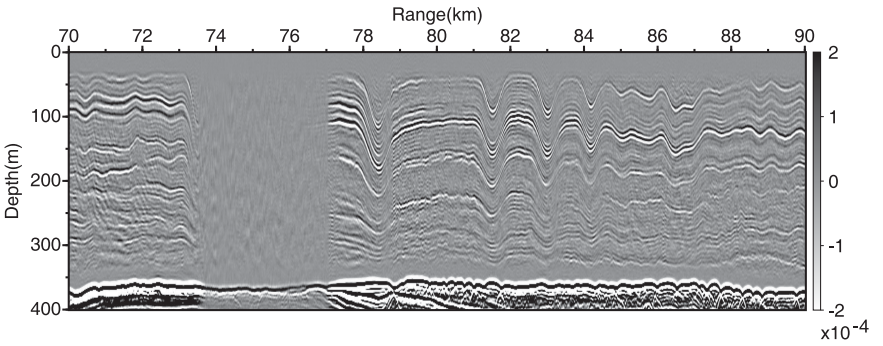

Figure 2. Seismic reflection coefficient image derived from the migrated multichannel seismic data of an ISW packet. Gray colors scale the amplitude of the acoustic reflectivity as shown on the color bar. The inverted results of 77–90 km are shown in Figure 7. The inverted potential density of 70–74 km is presented in Figure 14. The seabed was muted prior to migration to avoid unwanted noise from the seabed contaminating the water reflectivity then has been added back post migration.

reflectors and isothermals/isohalines are related. In hydrographic observations of the ISWs, temperature is a reliable proxy measurement for density, i.e., the isothermals and isopycnals are coincident [*Trevorrow*, 1998]. So most of the ISW observations directly use the isothermals to measure some the parameters of ISWs [e.g., *Ramp et al*., 2004; *Fu et al*., 2012]. Also, salinity and temperature are strongly correlated with almost identical fluctuation patterns [*Send and Baschek*, 2001; *Pawlowicz*, 2002; *Yang et al*., 2004]. From the seismic view, the acoustic reflections are primarily caused by temperature variations [*Ruddick et al*., 2009] and the reflections can be regarded as the isopycnals as long as they are not very deep for a vertically stratified water structure [*Tang et al*., 2014a]. Therefore, the seismic horizons could be carefully extracted and treated as the isothermals/isohalines of the water column. Such an approximation will be discussed later using synthetic modeling, since it is controversial and varies with different ocean conditions [*Biescas et al*., 2014].

Figure 4 shows the estimated salinity profiles and the improved initial models for inversion. The estimated standard deviations from the absolute differences using the neural network with validation data are below 0.1 psu and 0.02 psu at 60 m and 200 m, respectively. Having established a $(T,\ S,\ p)$ relationship, five XBT stations were used to construct the initial low frequency (<15 Hz) temperature and salinity models (supporting information Figure S1), from which an improved starting *T-S* model was constructed (Figures 4d and 4e) by stretching and compressing the long-wavelength components among the 6 picked main seismic horizons (Figure 4c).

3.3. MCMC Inversion

According to the stochastic Bayesian inference, an inversion problem is interpreted as a determination of the posterior distribution of the model parameters using a sampling algorithm [*Ulrych et al*., 2001]. In this paper, the Metropolis-Hastings sampling algorithm, which is a popular example of the MCMC approach, is used to sample the posterior distribution of model space through a random walk [*Mosegaard and Tarantola*, 1995].

Given a model $\boldsymbol{m}$ and data $\boldsymbol{d}$, Bayes' theorem provides a proportional expression to relate the prior $p(\boldsymbol{m})$ probability and posterior probability $p(\boldsymbol{m}|\boldsymbol{d})$ as follows:

$$p(\boldsymbol{m}|\boldsymbol{d}) \propto p(\boldsymbol{m}) \cdot L(\boldsymbol{m}|\boldsymbol{d}) \tag{3}$$

$$L(\boldsymbol{m}|\boldsymbol{d}) \propto \exp\left(-\sum \frac{\left(\boldsymbol{d}_{obs}-\boldsymbol{d}_{pred}\right)^2}{2\sigma_e^2}\right) \tag{4}$$

where $L(\boldsymbol{m}|\boldsymbol{d})$ is the likelihood function which is a measure of how good a model is in explaining the data [*Tarantola*, 2005], $\boldsymbol{d}_{obs}$ and $\boldsymbol{d}_{pred}$ are the observed data and forward predicted data, respectively, σ_e is the measured data uncertainty.

In this problem, a random sampler generates a proposed bivariate *T-S* model $\boldsymbol{m}^* = (T^*, S^*)$ from the current state $\boldsymbol{m}$ using the prior $p(\boldsymbol{m})$. By forward calculation, the fitness between the predicted data and observed

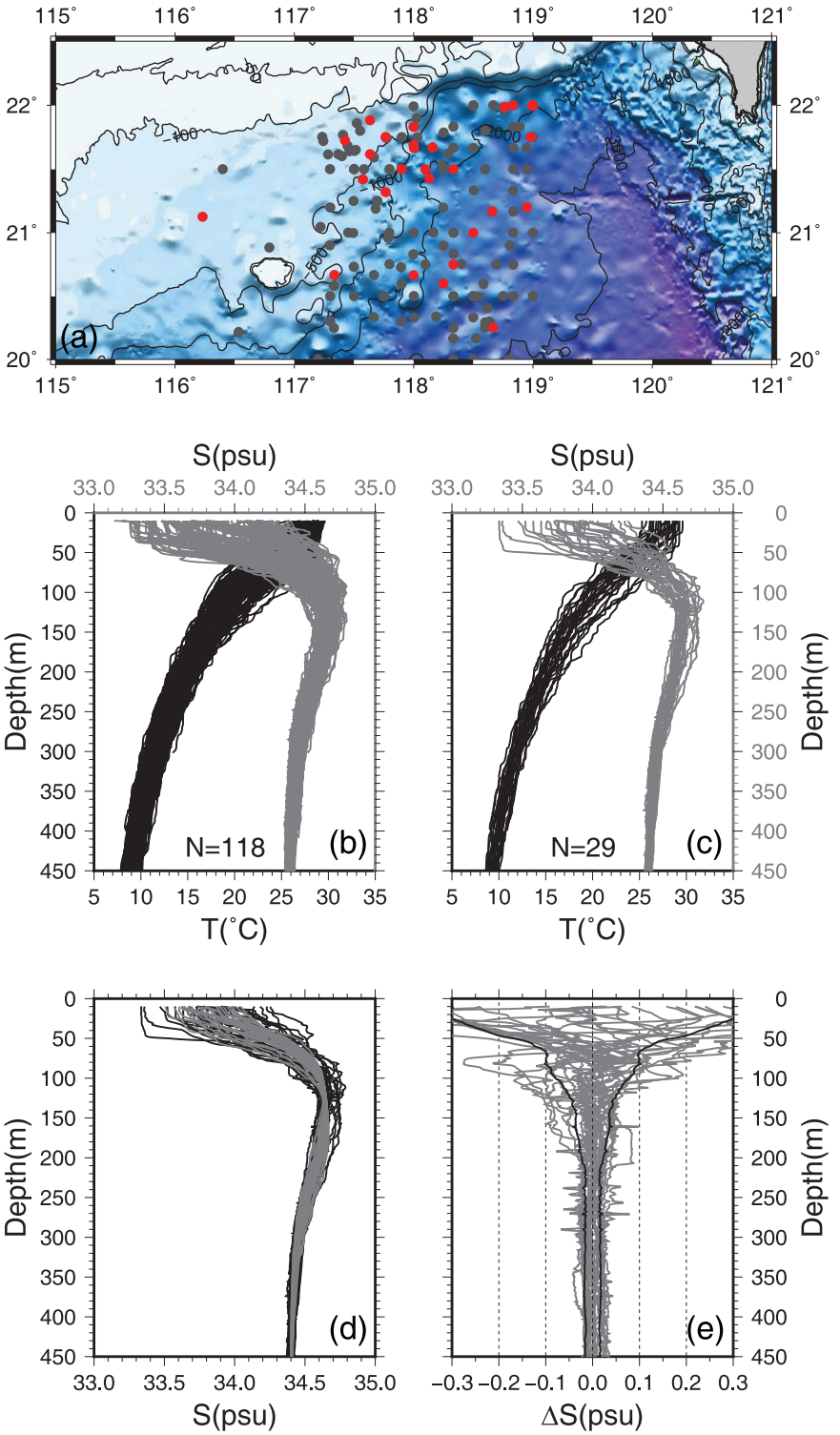

Figure 3. Derivation of *T-S* relation using neural network algorithm from the historical CTD casts. (a) Distribution of randomly selected CTD data for training (black, 80%) and validation (red, 20%). Temperature (black) and salinity (gray) profiles for (b) training and (c) validation. (d) Measured (black) and estimated (gray) salinity profiles. (e) Absolute differences (gray) and their standard deviations (black) between measured and estimated salinity profiles.

data are calculated as likelihood function $L(\boldsymbol{m}^*|\boldsymbol{d})$. The proposed model will be accepted if the new posterior probability is greater than the current posterior probability. Otherwise the proposed model may also be accepted but with a probability equal to a ratio between the proposed and current posterior probabilities,

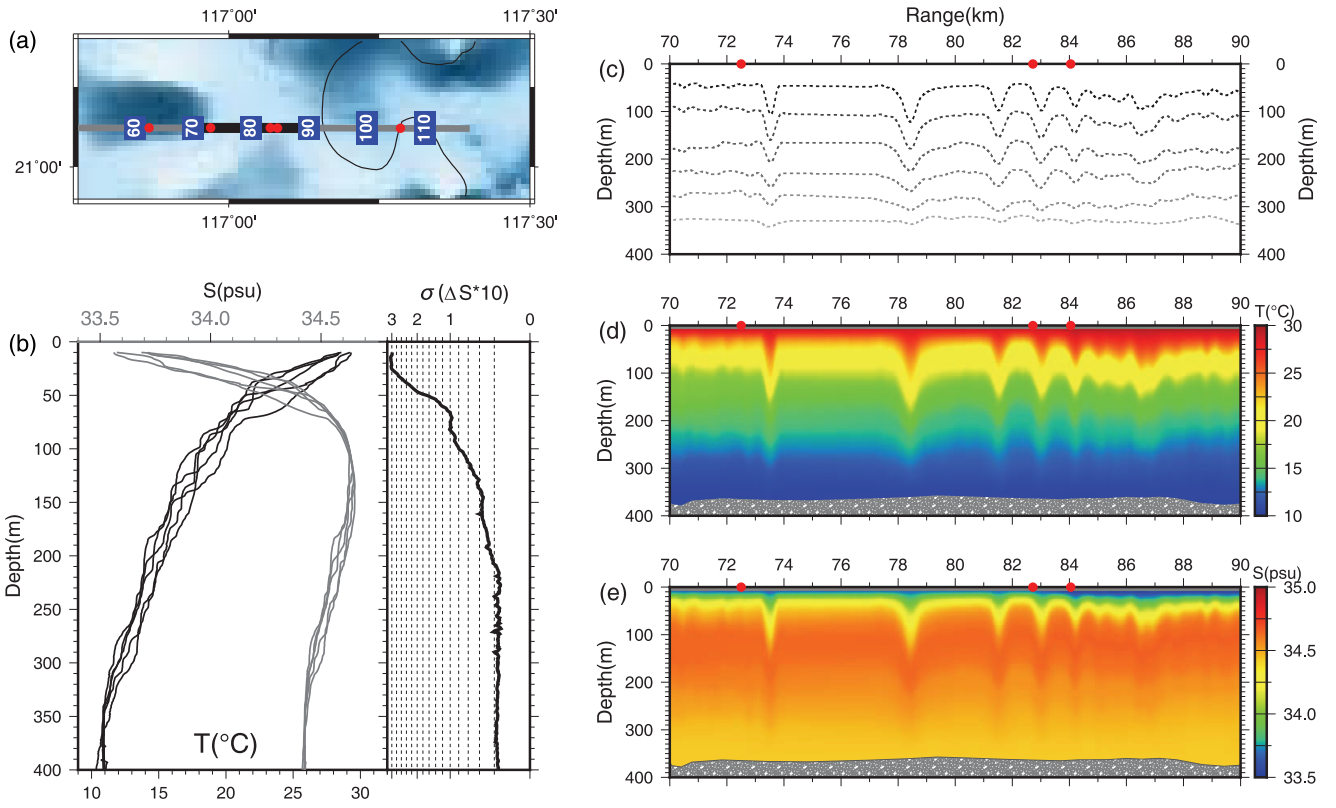

Figure 4. Estimated salinity profiles and improved initial models for inversions. (a) Seismic lines (gray) and 5 XBT stations (red dots). Three (two) of them are inside (outside) the concerned subsection between 70 and 90 km range (black). (b) (left) Temperature (black) and estimated salinity (gray) profiles. (right) The error of the neural network systems. (c) Main seismic reflections tracked from the seismic image (Figure 2). (d and e) The improved starting models of temperature and salinity, respectively, based on (c) the tracked seismic reflections and the smooth models shown in supporting information Figure S1.

allowing the process more fully sample the model space without getting trapped in local minima. Figure 5 provides a more intuitive illustration of how the Bayesian system works among prior, likelihood, and posterior distributions. The posterior is a joint distribution of the prior model and likelihood function.

It is assumed that the posterior or target distribution would be fully sampled via MCMC with a sufficient number of iterations *N*. After discarding the burn-in period, e.g., first 10% of *N*, the rest of sampled posterior is regarded as an approximation of the true model space which by statistical analysis can provide estimates of the means, uncertainties, and marginal distributions [*Martinez and Martinez*, 2002].

3.4. Model Parameterization

There are 3201 seismic traces that make up the 20 km seismic section with 6.25 m common midpoint (CMP) spacing (Figure 2). At each trace location a *T-S* model of water column is constructed with a 1 m depth interval. The prior information consists of the initial values and their uncertainties for the low frequency ($<$15 Hz) component of *T-S* structure from the interpolated models (Figures 4d and 4e) using 5 XBTs (Figures 3a and 3b) and 6 seismic horizons (Figure 4c). The prior $p(\boldsymbol{m})$ uncertainties in the form of a 2×2 covariance matrix from the prior model represented by a bivariate Gaussian probability density function (PDF). This is derived from the high frequency ($>$15 Hz) component of IMP result using a vertical moving window (15 m) scheme [*Gouveia and Scales*, 1998]. The covariance matrix provides information on the correlation between *T* and *S*. This *T-S* relationship, which is mandatory in other inversion methods, is not necessary if the MCMC inversion is fully data-driven. However, we chose to use it here to speed the convergence of the MCMC algorithm with the uncertainties in the *T-S* relationship in the off diagonal elements of the covariance matrix. The data (reflectivity) uncertainty in the likelihood function was estimated in the region (74–77 km) where there are no seismic reflectors, as representative of the ambient noise level (1.1×10^{-5}, SNR$\approx$5, defined as the RMS signal of the water reflection to RMS noise) of the reflectivity section. This will be overly

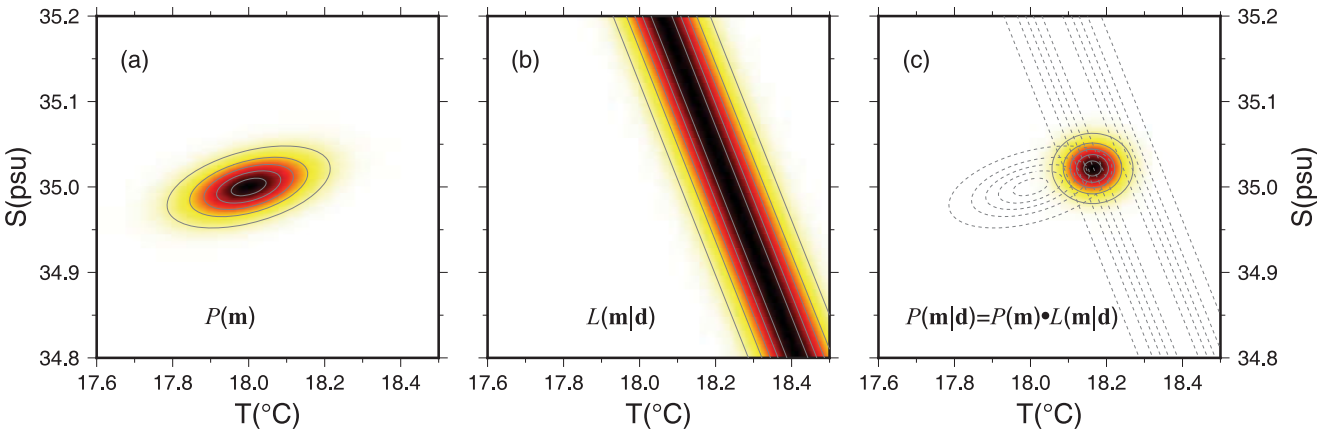

Figure 5. Illustration of how the Bayesian system works for *T-S* modeling in terms of probability density functions. The (c) posterior is the joint distribution of (a) prior and (b) likelihood.

pessimistic as in this region the streamer had been driven to the surface by the action of the leading ISW so was subject to excessive surface noise in this period.

For the MCMC inversion, the Markov chain length is $N=3000$, and the first 500 iterations are ignored as the burn-in. Analysis of the random walk showed that this chain length is more than suffice to ensure convergence of the MCMC inversion. At each depth-step on each profile, 3000 randomly proposed *T-S* pairs were generated with a step of up to one quarter of the standard deviations calculated from the variances in the covariance matrix. Only the samples passing the acceptance test within the Metropolis-Hastings (MH) algorithm were stored as the posteriors.

4. Results

Since this is the first time the MCMC approach is used to invert the *T-S* structure from the seismic data, we use two methods to corroborate this new approach. One is a synthetic test using data computed from a CTD cast. The other is the comparison of the inverted results between conventional linearized inversion and the MCMC approach. From these two tests, the nature of the MCMC approach is revealed together with its strengths and weaknesses.

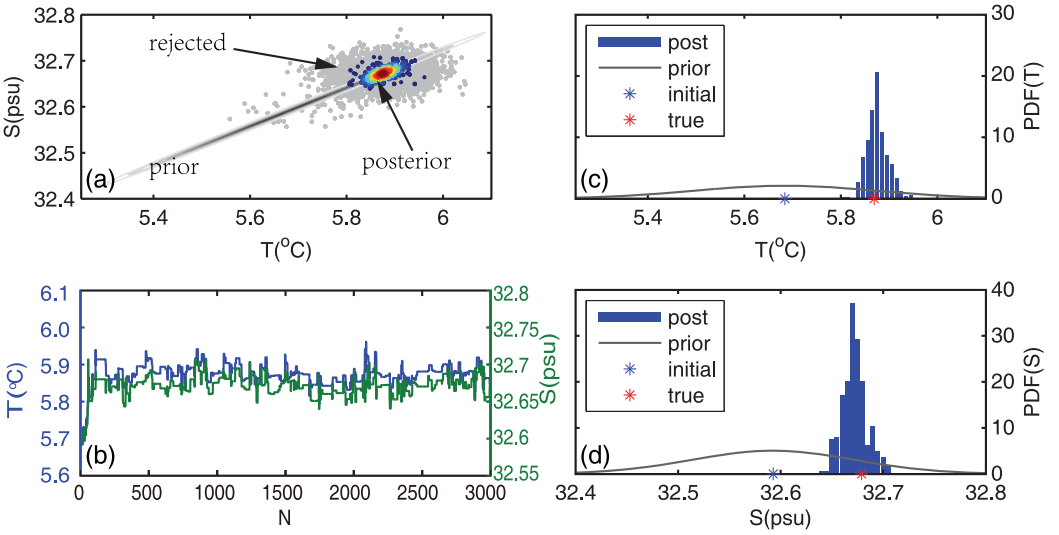

Figure 6. An example of Markov chains and probability functions of the MCMC approach for the synthetic modeling data. (a) Distributions of the rejected (gray dots) and accepted (color dots, post burn-in) samples. Gray contours are the prior information. (b) Markov chains of temperature (blue) and salinity (green). (c) Marginal distributions of the prior (gray line) and posterior (blue histogram) of temperature. Blue and red asterisks are the initial value and true value, respectively. (d) Same as Figure 6c but for salinity.

4.1. Test Inversion for a Synthetic Reflectivity Profile

A CTD cast centered on an anticyclonic eddy [*Tang et al*., 2014a, Figure 10, black star] was chosen for the synthetic modeling. It showed complex vertical variations with positive, negative, and near zero reflection series, covering most of the typical vertical features in the ocean. Such a choice of CTD profile will contribute to verifying the applicability of MCMC method for various ocean conditions. The acoustic reflection coefficients were calculated from the temperature, salinity, and depth profile using equation (1). The final reflectivity was the sum of a random noise sequence (SNR=5) and the synthetic reflectivity profile. Since the exact temperature and salinity are known, we can test the parameterization and evaluate the veracity of MCMC inversion.

The MCMC inverted results (supporting information Figure S5) show that the true data are centered on the posterior model spaces. *T* and *S* profiles are well recovered even though the synthetic reflectivity are contaminated with noise. The majority of the absolute *T* and *S* differences between the true quantities and inverted quantities are below 0.03°C and 0.03 psu, respectively. For the likelihood term of equation (4), the predicted reflectivity from the posterior models also fits the synthetic data. Their differences are within the data uncertainty.

In order to monitor how the MCMC is performing, we select a point at 106 m depth and extract the statistical parameters of mean, uncertainty, and correlation (Figure 6). Figure 6a shows the distribution of an entire Markov chain with both rejected and accepted samples. The posterior (accepted) samples are confined in a much narrower region than their prior distribution, which is an indication of convergence. The center of posterior has also moved away from the prior center (initial value). The trajectory of convergence is shown in Figure 6b. The Markov chain is quickly mixed after ∼100 iterations, much less than the burn-in we specified. For the marginal distributions of *T* and *S* (Figures 6c and 6d), the posterior PDFs are significantly improved compared to the prior information. Their uncertainties are reduced from 0.189°C to 0.022°C for temperature and from 0.079 psu to 0.012 psu for salinity. More importantly, the MCMC inversion found the solution (5.875°C, 32.672 psu) which is close to the true values (5.869°C, 32.679 psu) and away from the initial values (5.684°C, 32.592 psu).

4.2. MCMC Inversion for the Seismic Section

We applied the new developed MCMC inversion approach to the acoustic reflectivity section (Figure 2) to recover the depth range from 30 m to the seafloor. The seismic data were truncated above ∼30 m due to acquisition geometry. Recovered *T* and *S* models (mean of the posterior samples) along the section from 77 to 90 km are shown in Figure 7, as well as their uncertainties (standard deviation of the posterior samples). Having obtained the *T* and *S* models and their uncertainties, the corresponding physical characteristics, such as potential density and acoustic velocity, and their uncertainties were also derived.

The inverted sections show the high wavenumber *T-S* variations caused by the ISW train (Figures 7a and 7b). These *T-S* variations are fluctuating in the same pattern as the acoustic reflectivity, indicating that the variations are driven by the reflectivity during inversion. The contours of the *T-S* structures form the typical "sech^2" shape of the ISWs. With the improved initial model (Figure 4), this result is more credible than the simpler model based on straightforward interpolation of the XBT casts (supporting information Figure S1). Figure 8 shows the comparisons between the inverted results (black) and the in situ XBT measurements (red). We found that the recovered results fit well with the coincident oceanographic measurements.

The corresponding posterior uncertainties of the physical parameters were derived (Figures 7f–6j). There is a systematic pattern between the acoustic reflectivity and the model uncertainty which is consistent with our expectation. For instance, at a low-amplitude reflectivity point, the MCMC approach would preferentially accept the models with small *T-S* variations, hence a small uncertainty is estimated. And vice versa for the high-amplitude reflectivity points. Generally, most of the uncertainties for temperature, salinity, potential density, acoustic velocity, and impedance are less than 0.06°C, 0.006 psu, 0.02 kg/m^3, 0.2 m/s, and 200 kg/m^{2}s, respectively. The uncertainty patterns of potential density and acoustic velocity are more similar to the temperature than to the salinity, confirming that temperature is the dominant factor in density and velocity. Accordingly, variations of the acoustic velocity are the main contributions (∼90%) to the impedance variations (or reflectivity). This estimation is similar to the study by *Sallares et al*. [2009].

To look in more detail at the uncertainty variations, we first extracted the uncertainty profiles at three specific XBT locations (Figure 9). The uncertainties vary dramatically along each profile with an overall

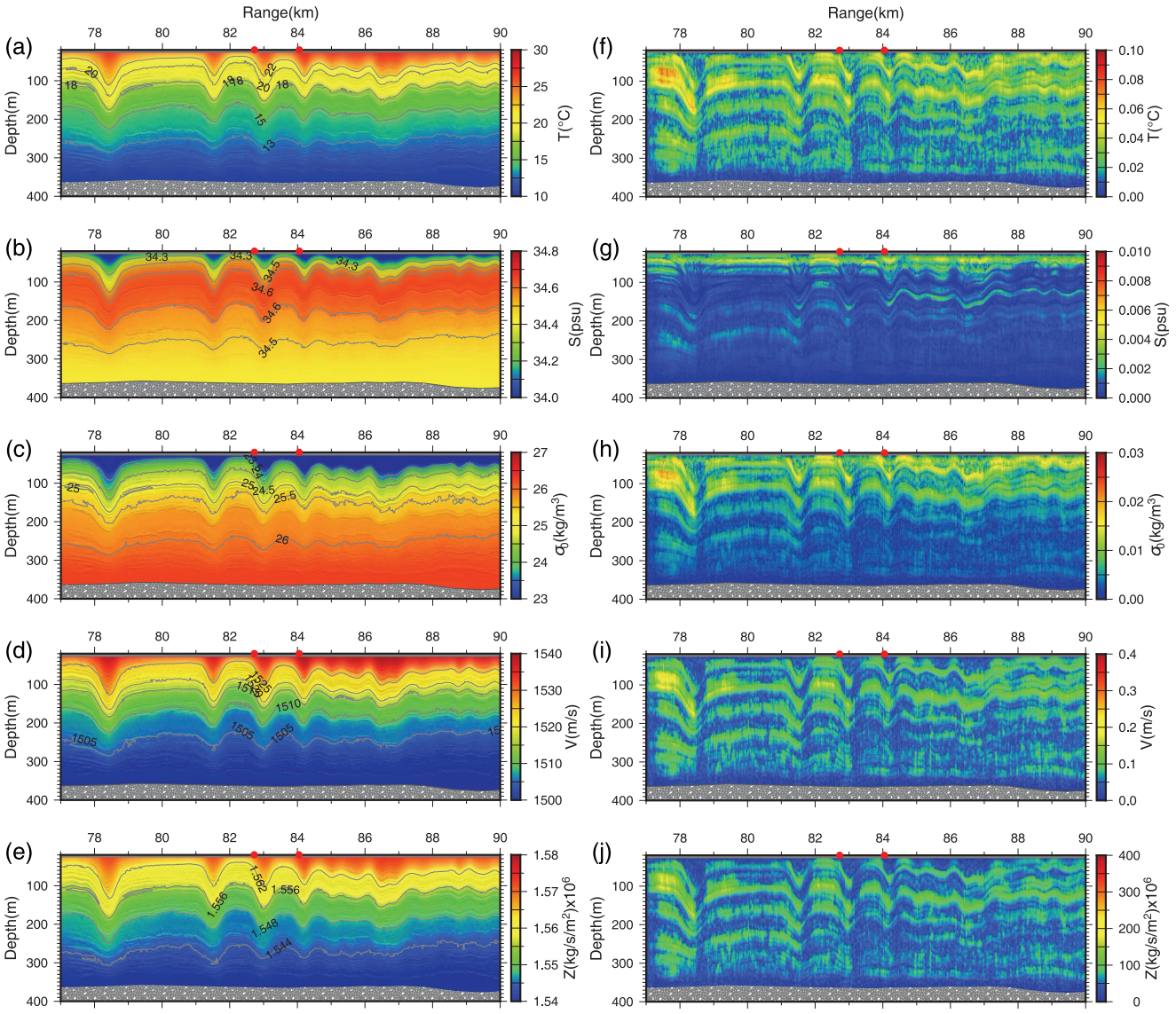

Figure 7. MCMC recovered (a) temperature, (b) salinity, (c) potential density, (d) acoustic velocity, and (e) acoustic impedance and (f–j) their corresponding posterior uncertainties from top to bottom using the improved starting model shown in Figure 4. The gray lines outline the contours of the retrieved quantities. Only 77–90 km range are presented showing the detailed structure of the rank-ordered ISW packet form the second soliton.

decreasing trend from shallow to deep water. Further, we investigated two representative MCMC sampling processes at points (77.5 km, 68 m depth) and (80.0 km, 68 m depth) away from any XBT control, where it is difficult to estimate uncertainty using previous methods, such as IMP method by *Biescas et al.* [2014]. This shortcoming can be compensated by using the MCMC approach. The Markov chain samplings are quickly mixed after few iterations and converge on specific values with highly focused posterior distributions (Figures 10a and 10d) and reduced uncertainties (Figures 10b, 10c, 10e, and 10f) compared to the prior information. Moreover, the Gaussian-like posterior distributions of the *T-S* samplings make us to believe that the hypothesis on the prior model with normal PDF is reasonable.

Similar to the supporting information Figure S5f, there should be self-consistency between the observed and the recovered reflectivity data and their residuals should be within the given range of SNR≈5. By calculating the reflectivity from the recovered *T-S* model, we derived a global mean difference of ∼10% of the data, which is typically lower than the noise level used in the likelihood function, indicating the MCMC method improved the confidence interval of the *T-S* model significantly after sufficient times of iteration.

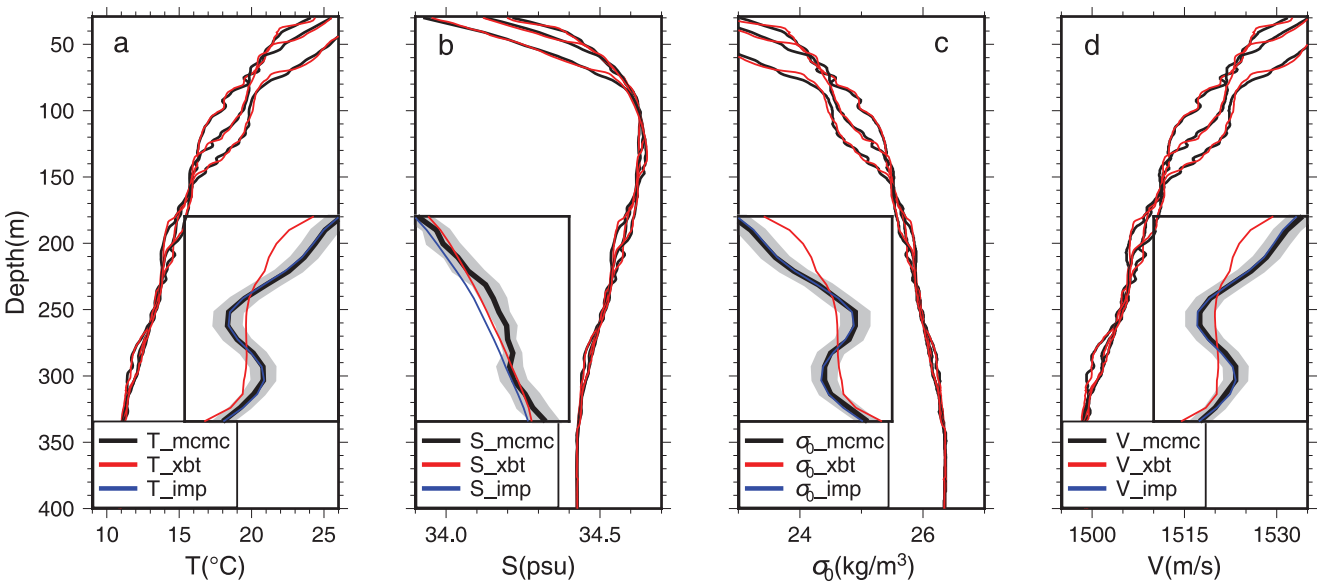

Figure 8. Comparisons between the in situ measurements (red) and recovered results (black) using MCMC method at three XBT sites. (a) Temperature; (b) salinity; (c) potential density; (d) acoustic velocity. The zoomed insets show the 95% confidential intervals (shaded) of each parameter estimated from MCMC method for one of the XBT sites. The window depths are ranging from 85 to 100 m and their widths are (a) 1°C, (b) 0.03 psu, (c) 0.25 kg/m^3, and (d) 3 m/s. The results from IMP method (blue) are also presented for comparison.

4.3. Comparisons to the Previous Method

To verify our result we recover temperature and salinity fields from the same acoustic reflectivity using a recently developed method (IMP) [*Biescas et al.*, 2014]. There are two main steps in the IMP approach. The first step is to recover the impedance model from acoustic reflectivity and low frequency impedance model, which is filtered and interpolated from XBT profiles (supporting information Figure S6). The second step is to search for the *T-S* pair, whose impedance is closest to the recovered impedance, using the *T-S* relation from the precalculated neural network table (supporting information Figure S4).

Using the IMP approach, the *T-S* fields (Figure 11) were inverted based on the improved starting model (Figure 4). These results are similar to those from the MCMC approach as shown in Figure 7, indicating consistency between the linearized and probabilistic methods.

More detailed differences between the inverted results and the in situ hydrographic measurements are shown in Figure 8 and Figure 12 for the XBT site at 82.7 km as an example. As shown in the insets of Figure 8, the retrieved results from both MCMC (black) and IMP (blue) are extremely close to each other except for the salinity. There are two implications can be drawn from this result. First, the salinity plays an insignificant role in the potential density or acoustic velocity. Second, the MCMC approach provides less restricted solutions than the IMP approach. The absolute differences between IMP/MCMC approaches and XBT measurements are shown in Figure 12. They have similar error levels overall and error trends vertically. The absolute difference between MCMC and IMP approaches (blue) are extremely small which is typically within the 95% confidence interval of the uncertainties (2-sigma in Figure 9). All these comparisons indicate the consistency and robustness of these two different inversion schemes.

5. Discussion

5.1. Features and Tips

An MCMC approach is developed to invert the *T-S* fields from the seismic reflection data based on the Bayesian inference. It proves to be effective both through a synthetic simulation test and by comparison with a conventional linearized inversion method. By applying this method to seismic reflection data of an ISW packet, the *T-S* fields are inverted and then other parameters are also estimated. The quantified uncertainties from the posterior samples make the MCMC method very promising.

Amplitude preservation is crucial. Even with our carefully constructed processing sequence, there is still a discrepancy between the amplitudes of seismic data and the hydrographic data above 100 m (supporting

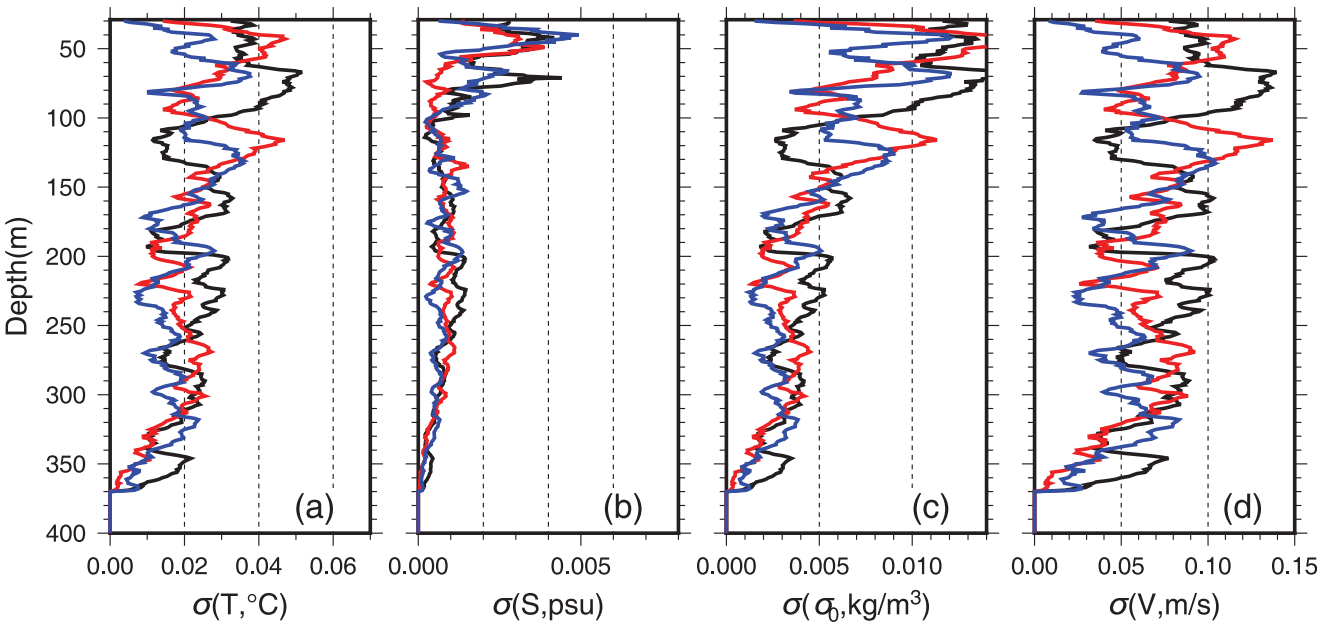

Figure 9. MCMC posterior uncertainties (σ) of (a) temperature, (b) salinity, (c) potential density (σ_0), and (d) acoustic velocity at three XBT sites on the subsection from left to right (Figure 4) as shown in black, red, and blue here.

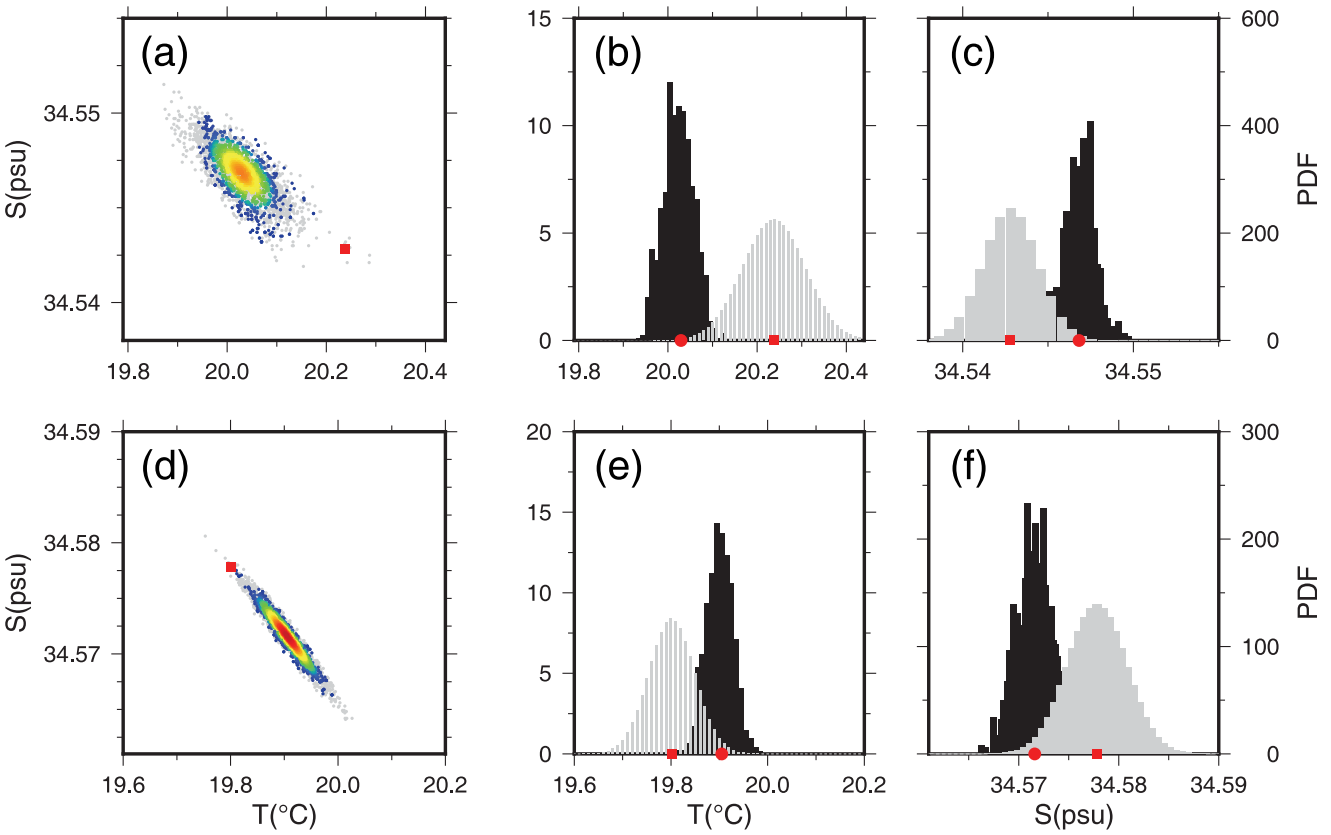

Figure 10. Examples of Markov chains and probability functions of the MCMC approach for acoustic reflectivity data at two points (77.5 km, 68 m; upper row) and (80.0 km, 68 m; lower row). (a, d) Distributions of the rejected (gray dots) and accepted (color dots, post burn-in) samples of the Markov chains. The colors of the dots represent the PDF of the bivariate normal distribution fit from the posteriors. Red squares are the initial values. (b, e) Marginal distributions of the prior (gray histogram) and posterior (black histogram) of temperature. Red dots and red squares are the posterior mean and initial values, respectively. (c, f) Same as Figures 10b and 10e but for salinity.

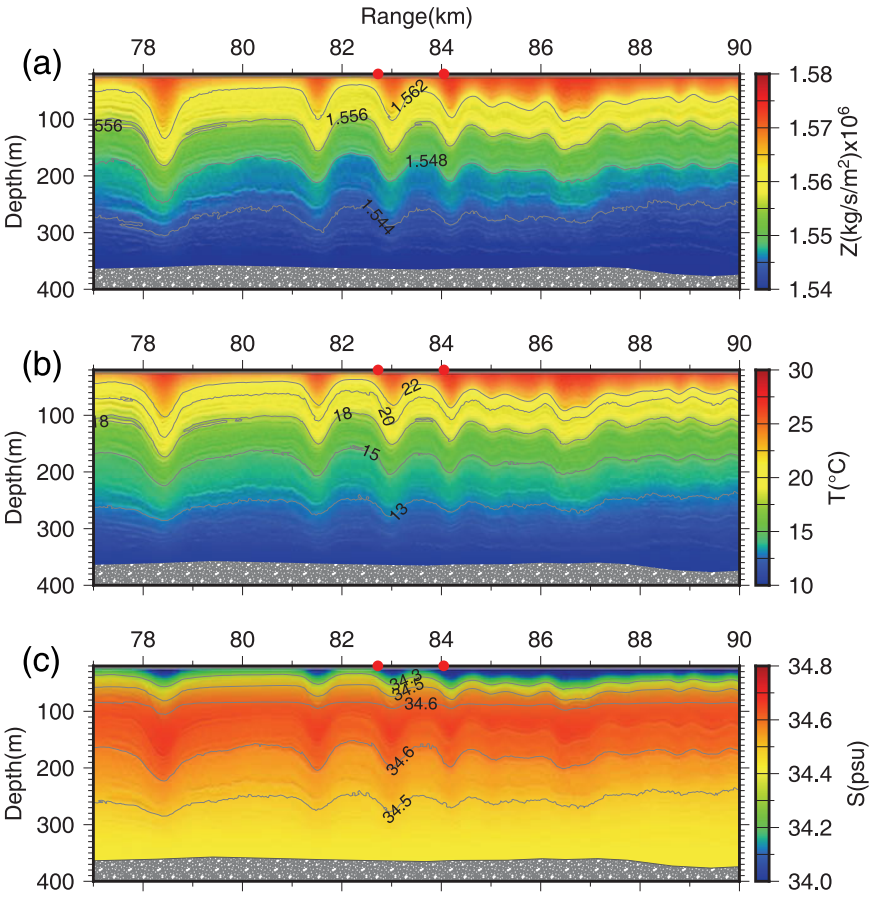

Figure 11. Inverted results using the IMP approach based on the seismically improved starting model (Figure 4). (a) Impedance. (b) Temperature. (c) Salinity.

information Figure S6d). An empirical correction factor could be introduced or certain steps of amplitude correction (supporting information Figure S2) need to be reconsidered.

The Doppler-effect of detecting the moving waves on a moving vessel will cause the reflections from the waves to be displaced and thus mis-stacked when using the conventional acquisition geometry and processing that assumes the waves are static [*Tang et al*., 2015, Figure 5]. This effect will blur the amplitude and distort signals [*Vsemirnova et al*., 2009] which is particularly noticeable on the flanks of the ISWs. A more considered approach to correcting the geometry for the moving waves shoulder improve the quality of imaging [*Klaeschen et al*., 2009].

Inherent errors of depth positioning from two different systems of seismic acquisition and XBT casts are inevitable, i.e., the difference between the inverted results and hydrographic observations are irreconcilable (supporting information Figure S6d). Therefore, using their difference as the inversion error is misleading whereas the posterior uncertainty from the MCMC is the optimal parameter to assess the solution reliability of the inversion method itself from the seismic data.

In the study, the uncertainty (error) of the salinity is lower than the previous studies [*Papenberg et al*., 2010; *Biescas et al*., 2014]. This is inherited from the neural network scheme used to derive the salinity for the XBT profiles which smooth the variations and thus underestimate the prior and posterior uncertainties. However, without coincident CTD data this scheme is a plausible method to estimate the unknown salinity. The performance of the salinity uncertainty is examined by the estimation from the synthetic modeling in section 4.1.

We have tested the inversion approach with several different prior uncertainty models, e.g., from XBTs or from IMP inverted models. We find that when the prior uncertainty was not well estimated, the posterior

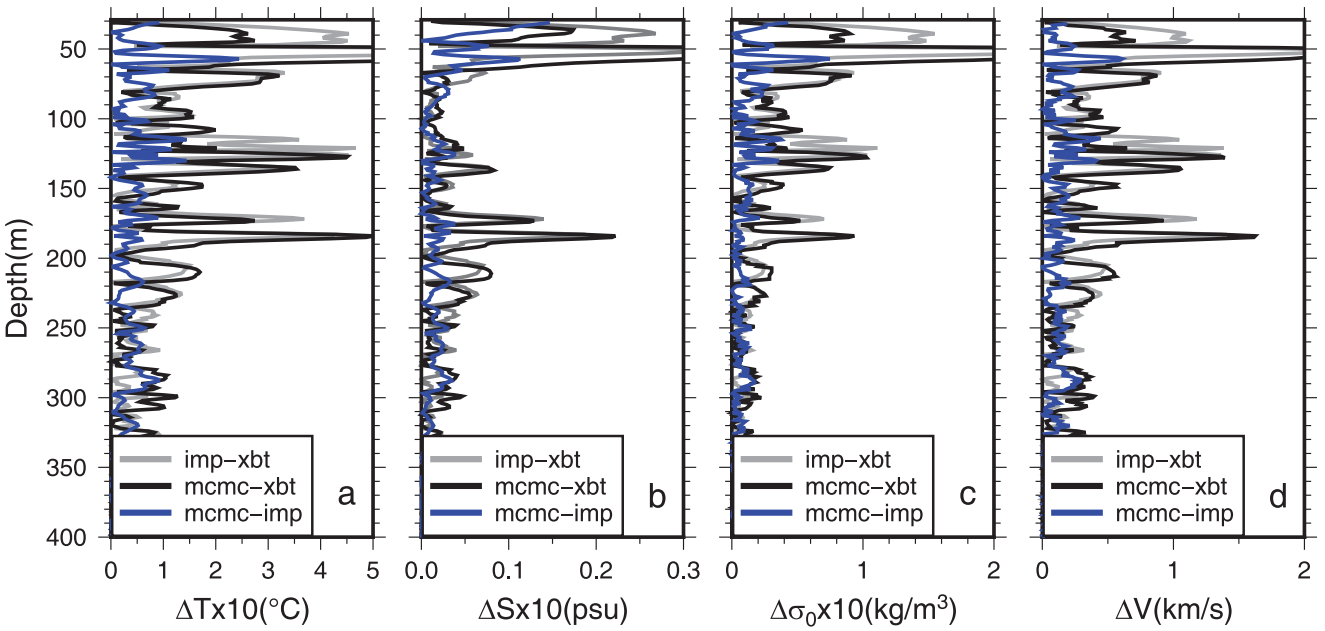

Figure 12. An example shows the absolute differences between the inverted results and hydrographic observations of XBT profiles at 82.7 km: IMP-XBT (gray); MCMC-XBT (black); and MCMC-IMP (blue). (a) Temperature. (b) Salinity. (c) Potential density. (d) Acoustic velocity. Note this does not represent the error of the seismic inversion as it is likely that there is a depth mismatch between the XBT measurement and the inversion result.

uncertainty which is not purely data-driven will also change the patterns according the equation (3). However, the *T-S* models were still well recovered, indicating the robustness of the MCMC approach.

The ambient noise within the acoustic reflectivity is another factor affecting the inversion result. To reduce its effect, it is possible to combine the adjacent traces of reflectivity, e.g., moving window scheme, and invert one model. This would be applicable only if the lateral variance in the time of the reflection is small. In this study, the flanks of ISWs are too steep to be regarded as one model within a 60 m window (10 CMP traces), for example, though this strategy may succeed on other data.

In general, the band-limited high-frequency seismic signal cannot recover the long wavelength variability in the ocean unless the seismic travel times are included [*Wood et al*., 2008]. Spatially improved starting models are required to compensate for this deficiency. Vertically, the long wavelength in situ hydrographic measurements can be used as the background. Laterally, the seismic horizons can be used to define the isothermals or isohalines of the ISWs extending from hydrographic sites as we have done in this study.

The MCMC method is time consuming comparing to the IMP method ($\sim 10^3$ times slower). However, the MCMC method provides a means for assessing the reliability of the recovered result as it provides quantified uncertainties along the whole inversion section for every physical characteristic, whether their relations are linear or nonlinear. Though it is reassuring that the error in the IMP method is similar to the MCMC where there is hydrographic calibration (Figure 12), the IMP method cannot provide a reliable estimate of uncertainty which can lead to overconfidence in the result.

5.2. Isothermal Approximation

For the improved model (Figure 4), we assumed that the seismic reflectors are consistent to the isothermals/isohalines. However, according to the recent study [*Biescas et al*., 2013], this assumption is controversial and might be misleading under some circumstance since the isopycnals of potential density do not always follow the seismic reflectors. Thus a question arises: how valid is this assumption for the ISWs? To address this question, an ISW model with amplitude of 80 m is created under an adiabatic assumption or potential temperature conservation along the ISW surfaces [*Vlasenko et al*., 2005] to compare the difference between the seismic reflectors and the contours of temperature, salinity, velocity, (in situ) density, potential density, etc.

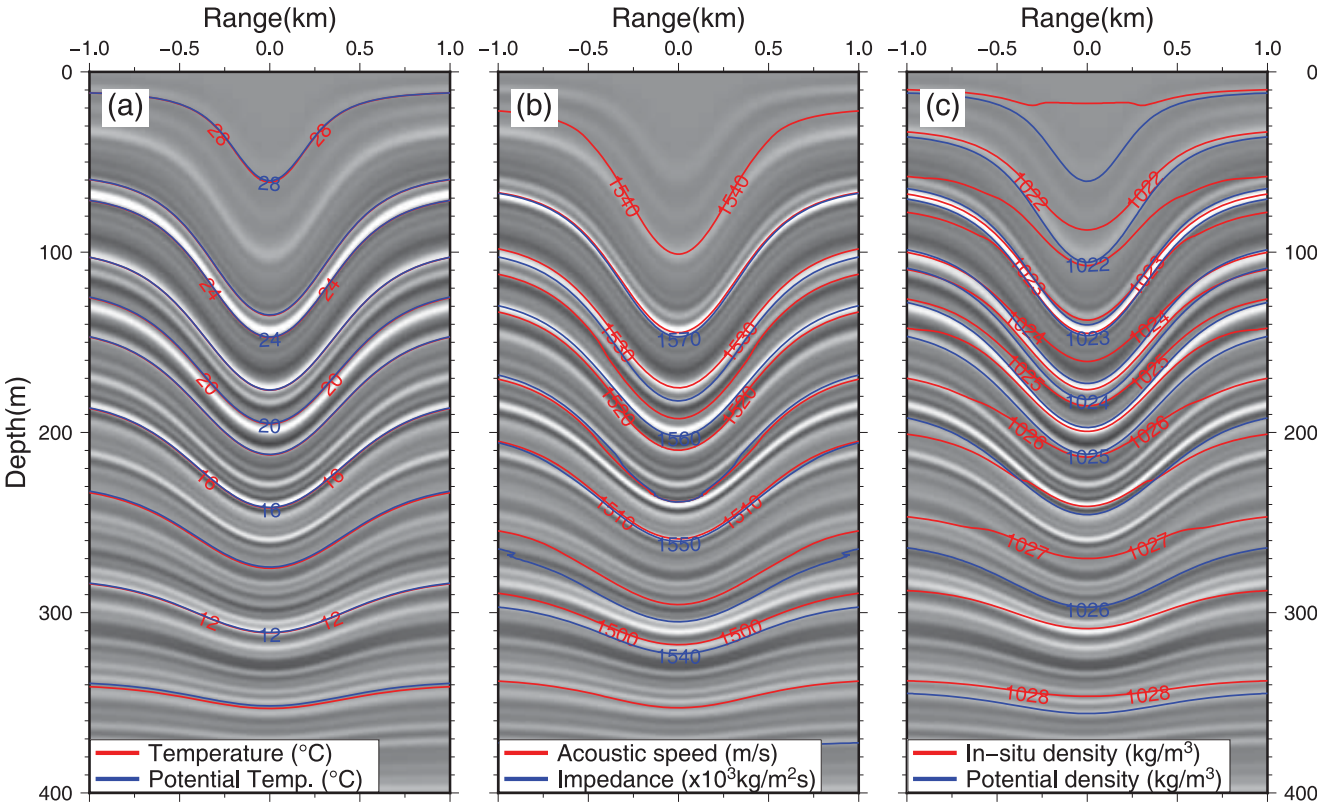

Figure 13. Synthetic modeling of the seismic image (gray background) and the physical fields (contours) of an ISW. (a) Temperature (red) and potential temperature (blue) contours. (b) Acoustic velocity (red) and impedance (blue). (c) In situ density (red) and potential density (blue) contours.

The synthetic result shows that the seismic reflectors are in accordance with isothermals of both in situ temperature and potential temperature (Figure 13a). However, the displacements between the velocity contours and the reflectors or isothermals can reach to ∼20% of the ISW amplitude (Figure 13b), but typically they are small, e.g., near contours 1530–1535. The acoustic impedance follows the velocity very well but not the impedance contrasts or the reflectors (Figure 13b). The differences between the seismic reflectors and the contours of (in situ) density are significant (Figure 13c). They may be occasionally up to 50% of the ISW amplitude. However, there is a perfect match for the isopycnals of potential density (Figure 13c).

We conclude that for the ISWs, the seismic reflectors could be a useful substitute for the isothermals or isopycnals of potential density. Therefore we believe that our approach to improve our initial model (Figure 4) is justified. Nevertheless, it is somewhat surprising that the contours of three parameters acoustic velocity, in situ density, and acoustic impedance from which the seismic responses are derived, are not consistent to the seismic reflectors themselves.

5.3. Isopycnal Stirring and Diapycnal Mixing

The oceanic ISW is considered to be a typical sub-mesoscale stirring process, which is reversible [*Shcherbina et al.*, 2014]. For the well-developed solitons, they were always symmetrically restored to their initial states quickly (Figure 7). It took a bit longer for the quasilinear internal waves at the dispersing tail (∼84–90 km) to restore. The mixed layer subsided from ∼40 m to 60 m depth and then uplifted toward the initial states again within less than 6 km.

Assuming the initial vertical stratification along the whole seismic section is uniform, we compared the initial and final states of the water column after the passage of the ISW packet (Figure 14a). The general stratification is changed significantly. The mixed layer is thickened while the thermocline is thinned. These phenomena are very similar to the previous observation by *Ramp et al.* [2004]. The internal tidal bores, which the ISWs are usually riding on, might be responsible for the low frequency variances. Meanwhile, the

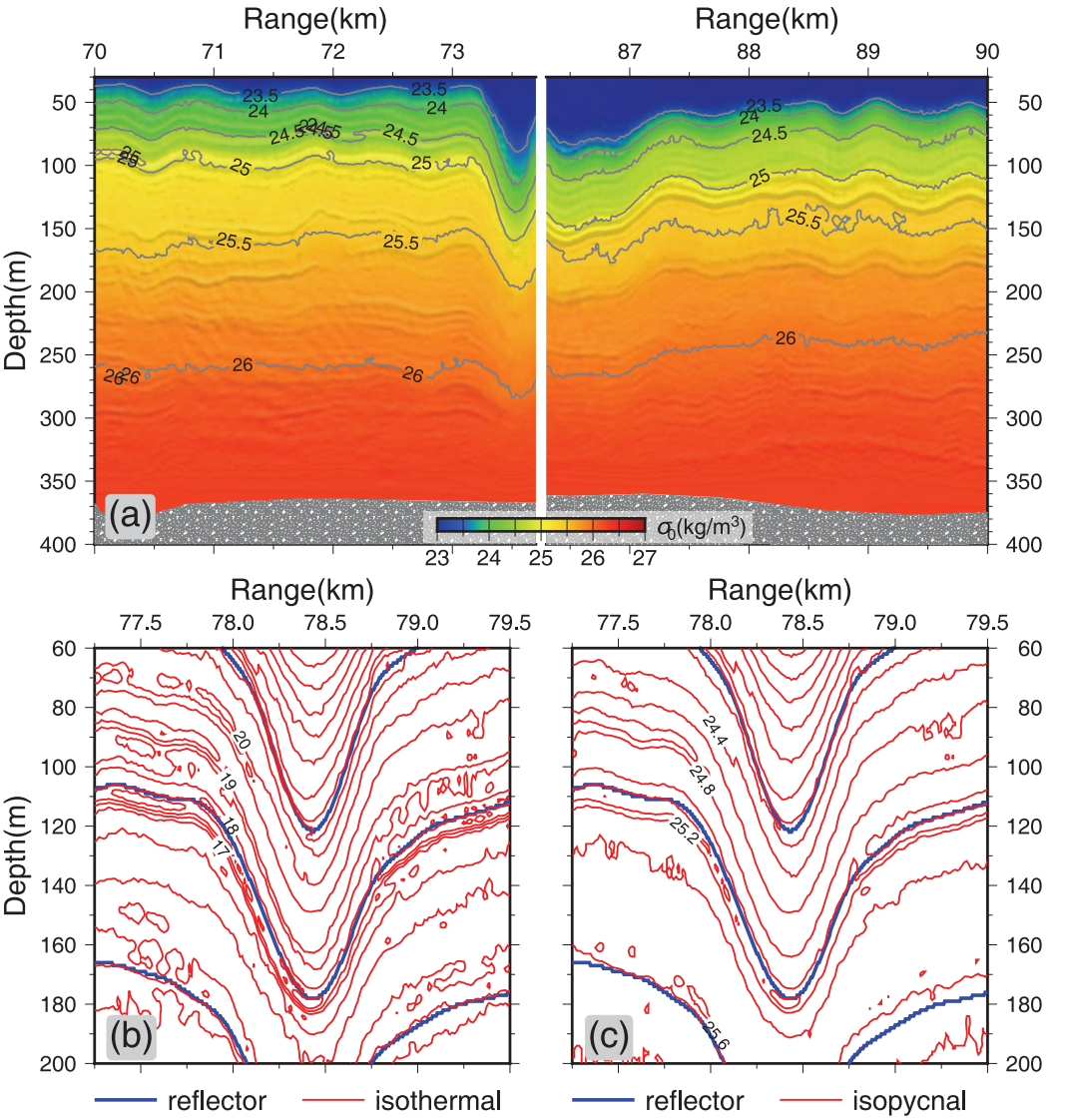

Figure 14. (a) Potential density (left) before and (right) after the passage of ISW packet. (b) Finescale structure of the second soliton with primary reflectors (blue) and isothermals (red). (c) Same as Figure 14b but for the isopycnals.

integrated effect of the passing ISW packet may also change the stratification [*Semin et al*., 2014] via reversible stirring and then irreversible diapycnal mixing.

Figures 14b and 14c depict the finescale temperature and density contours of the second soliton, respectively, as well as the main reflectors. Variations along and across the isothermals and isopycnals are shown. Small patches of thermal anomalies are observed intervening among the background isothermals near the main reflectors. These anomalies are typically longer than 30 m of the lateral resolution according to the first Fresnel zone and stronger than the uncertainty of our estimation to a 95% confidence interval. A series of small scale unstable phenomena as stirring, interleaving, detaching, and breaking can be distinguished. Some details are difficult to distinguish without sufficient vertical samples using the hydrographic mooring array with relative sparse sensors (>10 m) [*Ramp et al*., 2004]. Local instabilities can also be noted from the vertical temperature/density inversions both preceding and following the arrival of soliton (Figures 14b an 14c), where the diapycnal mixing tends to occur. Such overturns had been observed by the simultaneous CTD profiling of the passing ISW packets [*Pinkel*, 2000]. The highly sheared flow triggered by the ISWs might be responsible for the unstable overturns and thereafter vertical turbulent mixing. Apparently, ISWs play effective roles in modification of the water properties from sub-mesoscale to finescale. Therefore, a further

quantified description of the mixing and diffusion would be a very interesting and challenging topic, but beyond the scope of this study.

6. Conclusions

This work explores a new application of a Markov Chain Monte Carlo (MCMC) approach to recover the temperature and salinity of ISW field using the seismic reflectivity data and simultaneous hydrographic data. An MCMC approach was designed for directly sampling the posterior probability distribution of temperature and salinity which are the solutions of the system under investigation. The primary improvement is the capability of incorporating uncertainties in observations and prior models which then provide quantified uncertainties for the posterior model. Synthetic modeling shows that the MCMC approach quickly finds the temperature and salinity solutions within the significantly narrowed down confidence intervals of 0.03°C and 0.03 psu, respectively. And the statistically derived results of ISW field is equivalent to the conventional linearized inversion method. While the former provides us the quantified uncertainties of the recovered temperature (0.06°C) and salinity (0.006 psu) along the whole section the latter does not.

Similar to other conventional methods, an accurate starting model is necessary to compensate the missing low frequency information of the seismic data, especially for the sub-mesoscale variations in this study. Seismic reflectors are incorporated to refine the starting model, through which the MCMC method derives a reliable finescale temperature, salinity, acoustic velocity, and density of ISW field, as well as their uncertainties. These results are the first time ISWs have been mapped with sufficient detail for further analysis of their dynamic properties.

Acknowledgments

We thank the captain, crew, and science party (Y.L. Wang; H.B. Zheng; J.C. Zhang) of R/V *SHIYAN2* for acquiring the seismic data and XBT data funded by the NSFC Open Research Cruise of Geophysics NORC2014-08. Warren T Wood and an anonymous reviewer are greatly acknowledged for their constructive comments and suggestions. Data are available for academic research on request to the author QT (tqsh@scsio.ac.cn). This research was supported financially by the NSFC (grants 41376023 and 41176026), Youth Innovation Promotion Association CAS, and also partially supported by Chinese Scholarship Council (201408440021) for a visit by QT to Durham University. Berta Biescas' work has been funded by the European Commission through a Marie Curie Action FP7-PEOPLE-2012-COFUND-600407.

References

Ballabrera-Poy, J., B. Mourre, E. Garcia-Ladona, A. Turiel, and J. Font (2009), Linear and non-linear T-S models for the eastern North Atlantic from Argo data: Role of surface salinity observations, *Deep Sea Res., Part I*, *56*(10), 1605–1614, doi:10.1016/j.dsr.2009.05.017.

Biescas, B., B. Ruddick, and V. Sallares (2013), Inversion of density in the ocean from seismic reflection data, *J. Acoust. Soc. Am.*, *133*(5), 3312, doi:10.1121/1.4805509.

Biescas, B., B. R. Ruddick, M. R. Nedimovic, V. Sallares, G. Bornstein, and J. F. Mojica (2014), Recovery of temperature, salinity, and potential density from ocean reflectivity, *J. Geophys. Res. Oceans*, *119*, 3171–3184, doi:10.1002/2013JC009662.

Bornstein, G., B. Biescas, V. Sallarès, and J. F. Mojica (2013), Direct temperature and salinity acoustic full waveform inversion, *Geophys. Res. Lett.*, *40*, 4344–4348, doi:10.1002/grl.50844.

Buijsman, M. C., Y. Kanarska, and J. C. McWilliams (2010), On the generation and evolution of nonlinear internal waves in the South China Sea, *J. Geophys. Res.*, *115*, C02012, doi:10.1029/2009JC005275.

Cai, S., J. Xie, and J. He (2012), An overiew of internal solitary waves in the South China Sea, *Surv. Geophys.*, *33*(5), 927–943, doi:10.1007/s10712-012-9176-0.

Cai, S. Q., S. G. Wang, and X. M. Long (2006), A simple estimation of the force exerted by internal solitons on cylindrical piles, *Ocean Eng.*, *33*(7), 974–980, doi:10.1016/j.oceaneng.2005.05.012.

Fu, K. H., Y. H. Wang, L. St Laurent, H. Simmons, and D. P. Wang (2012), Shoaling of large-amplitude nonlinear internal waves at Dongsha Atoll in the northern South China Sea, *Cont. Shelf Res.*, *37*, 1–7, doi:10.1016/j.csr.2012.01.010.

Gouveia, W. P., and J. A. Scales (1998), Bayesian seismic waveform inversion: Parameter estimation and uncertainty analysis, *J. Geophys. Res.*, *103*(B2), 2759–2779, doi:10.1029/97JB02933.

Holbrook, W. S., P. Paramo, S. Pearse, and R. W. Schmitt (2003), Thermohaline fine structure in an oceanographic front from seismic reflection profiling, *Science*, *301*(5634), 821–824.

Huang, X. D., W. Zhao, J. W. Tian, and Q. X. Yang (2014), Mooring observations of internal solitary waves in the deep basin west of Luzon Strait, *Acta Oceanol. Sin.*, *33*(3), 82–89.

Jones, I. F., and S. Levy (1987), Signal-to-noise ratio enhancement in multichannel seismic data via the Karhunen-Loeve transform, *Geophys. Prospect.*, *35*(1), 12–32, doi:10.1111/j.1365-2478.1987.tb00800.x.

Klaeschen, D., R. W. Hobbs, G. Krahmann, C. Papenberg, and E. Vsemirnova (2009), Estimating movement of reflectors in the water column using seismic oceanography, *Geophys. Res. Lett.*, *36*, L00D03, doi:10.1029/2009GL038973.

Kormann, J., B. Biescas, N. Korta, J. de la Puente, and V. Sallares (2011), Application of acoustic full waveform inversion to retrieve high-resolution temperature and salinity profiles from synthetic seismic data, *J. Geophys. Res.*, *116*, C11039, doi:10.1029/2011JC007216.

Lien, R.-C., F. Henyey, B. Ma, and Y. J. Yang (2014), Large-Amplitude Internal Solitary Waves Observed in the Northern South China Sea: Properties and Energetics, *J. Phys. Oceanogr.*, *44*(4), 1095–1115, doi:10.1175/JPO-D-13-088.1.

Martinez, W. L., and A. R. Martinez (2002), *Computational Statistics Handbook With MATLAB*, 591 pp., Chapman and Hall, Boca Raton, Fla.

Millero, F. J. (2010), History of the equation of state of seawater, *Oceanography*, *23*(3), 18–33.

Mosegaard, K., and A. Tarantola (1995), Monte-Carlo sampling of solutions to inverse problems, *J. Geophys. Res.*, *100*(B7), 12,431–12,447, doi:10.1029/94JB03097.

Orr, M. H., and P. C. Mignerey (2003), Nonlinear internal waves in the South China Sea: Observation of the conversion of depression internal waves to elevation internal waves, *J. Geophys. Res.*, *108*(C3), 3064, doi:10.1029/2001JC001163.

Padhi, A., S. Mallick, W. Fortin, W. S. Holbrook, and T. M. Blacic (2015), 2-D ocean temperature and salinity images from pre-stack seismic waveform inversion methods: An example from the South China Sea, *Geophys. J. Int.*, *202*, 800–810, doi:10.1093/gji/ggv188.

Papenberg, C., D. Klaeschen, G. Krahmann, and R. W. Hobbs (2010), Ocean temperature and salinity inverted from combined hydrographic and seismic data, *Geophys. Res. Lett.*, *37*, L04601, doi:10.1029/2009GL042115.

Pawlowicz, R. (2002), Observations and linear analysis of sill-generated internal tides and estuarine flow in Haro Strait, *J. Geophys. Res.*, *107*(C6), 3056, doi:10.1029/2000JC000504.
Pinkel, R. (2000), Internal solitary waves in the warm pool of the western equatorial Pacific, *J. Phys. Oceanogr.*, *30*(11), 2906–2926.
Ramp, S. R., and T. Y. Tang (2011), A history of Taiwan/US oceanographic research in the South China Sea, *Oceanography*, *24*(4), 16–23, doi:10.5670/oceanog.2011.90.
Ramp, S. R., T. Y. Tang, T. F. Duda, J. F. Lynch, A. K. Liu, C. S. Chiu, F. L. Bahr, H. R. Kim, and Y. J. Yang (2004), Internal solitons in the northeastern South China Sea - Part I: Sources and deep water propagation, *IEEE J. Oceanic Eng.*, *29*(4), 1157–1181, doi:10.1109/JOE.2004.840839.
Ruddick, B., H. B. Song, C. Z. Dong, and L. Pinheiro (2009), Water column seismic images as maps of temperature gradient, *Oceanography*, *22*(1), 192–205.
Sacchi, M. D. (1997), Reweighting strategies in seismic deconvolution, *Geophys. J. Int.*, *129*(3), 651–656.
Sallares, V., B. Biescas, G. Buffett, R. Carbonell, J. J. Danobeitia, and J. L. Pelegri (2009), Relative contribution of temperature and salinity to ocean acoustic reflectivity, *Geophys. Res. Lett.*, *36*, L00D06, doi:10.1029/2009GL040187.
Semin, S., O. Kurkina, A. Kurkin, T. Talipova, E. Pelinovsky, and E. Churaev (2014), Features of fluid flows in strongly nonlinear internal solitary waves, *Nonlinear Processes Geophys. Discuss.*, *1*, 1919–1946.
Send, U., and B. Baschek (2001), Intensive shipboard observations of the flow through the Strait of Gibraltar, *J. Geophys. Res.*, *106*(C12), 31,017–31,032.
Shcherbina, A. Y., et al. (2014), The LatMix Summer Campaign: Submesoscale stirring in the upper ocean, *Bull. Am. Meteorol. Soc.*, doi:10.1175/BAMS-D-14-00015.1.
Sheriff, R. E., and L. P. Geldart (1995), *Exploration Seismology*, 2nd ed., 592 pp., Cambridge Univ. Press, Cambridge, U. K.
Tang, Q. S., S. P. S. Gulick, and L. T. Sun (2014a), Seismic observations from a Yakutat eddy in the northern Gulf of Alaska, *J. Geophys. Res. Oceans*, *119*, 3535–3547, doi:10.1002/2014JC009938.
Tang, Q. S., C. X. Wang, D. X. Wang, and R. Pawlowicz (2014b), Seismic, satellite, and site observations of internal solitary waves in the NE South China Sea, *Sci. Rep.*, *4*, 5374, doi:10.1038/srep05374.
Tang, Q. S., R. W. Hobbs, D. X. Wang, L. T. Sun, C. Zheng, J. B. Li, and C. Z. Dong (2015), Marine seismic observation of internal solitary wave packets in the northeast South China Sea, *J. Geophys. Res. Oceans*, *120*, 8487–8503, doi:10.1002/2015JC011362.
Tarantola, A. (2005), *Inverse Problem Theory and Methods for Model Parameter Estimation*, 342 pp., Soc. for Ind. and Appl. Math., Philadelphia, Penn.
Trevorrow, M. V. (1998), Observations of internal solitary waves near the Oregon coast with an inverted echo sounder, *J. Geophys. Res.*, *103*(C4), 7671–7680.
Ulrych, T. J., M. D. Sacchi, and A. Woodbury (2001), A Bayes tour of inversion: A tutorial, *Geophysics*, *66*(1), 55–69, doi:10.1190/1.1444923.
Vlasenko, V., L. Ostrovsky, and K. Hutter (2005), Adiabatic behavior of strongly nonlinear internal solitary waves in slope-shelf areas, *J. Geophys. Res.*, *110*, C04006, doi:10.1029/2004JC002705.
Vsemirnova, E., R. Hobbs, N. Serra, D. Klaeschen, and E. Quentel (2009), Estimating internal wave spectra using constrained models of the dynamic ocean, *Geophys. Res. Lett.*, *36*, L00D07, doi:10.1029/2009GL039598.
Warner, M. (1990), Absolute reflection coefficients from deep seismic reflections, *Tectonophysics*, *173*(1-4), 15–23, doi:10.1016/0040-1951(90)90199-I.
Wood, W. T., W. S. Holbrook, M. K. Sen, and P. L. Stoffa (2008), Full waveform inversion of reflection seismic data for ocean temperature profiles, *Geophys. Res. Lett.*, *35*, L04608, doi:10.1029/2007GL032359.
Yang, Y. J., T. Y. Tang, M. H. Chang, A. K. Liu, M. K. Hsu, and S. R. Ramp (2004), Solitons northeast of Tung-Sha Island during the ASIAEX pilot studies, *IEEE J. Oceanic Eng.*, *29*(4), 1182–1199, doi:10.1109/Joe.2004.841424.
Zhang, P., S. Tang, K. Qu, and Q. Zhang (2012), Test and analysis on domestic-made XBT probe, *Tech. Acoust.*, *31*(6), 570–573.
Zhao, Z. X., V. Klemas, Q. N. Zheng, and X. H. Yan (2004), Remote sensing evidence for baroclinic tide origin of internal solitary waves in the northeastern South China Sea, *Geophys. Res. Lett.*, *31*, L06302, doi:10.1029/2003GL019077.
Zheng, Q., R. D. Susanto, C. R. Ho, Y. T. Song, and Q. Xu (2007), Statistical and dynamical analyses of generation mechanisms of solitary internal waves in the northern South China Sea, *J. Geophys. Res.*, *112*, C03021, doi:10.1029/2006JC003551.